Materials Today Nano 36 (2026) 100972

Contents lists available at ScienceDirect

Materials Today Nano

journal homepage: www.sciencedirect.com/journal/materials-today-nano

Plasmon-activated hydrogen gas sensor based on $Au_{nanorod}$@ZnO core-shell structure nanoparticles operating at room temperature

Tuong Van Tran [a,b], Dong-Seog Kim [c], Geun-Jae Oh [c], Bharagav Urupalli [c], Hyeonseol Kim [d], Hee-Yeoun Kim [d], Dae-Hee Won [e,*], Yeon-Tae Yu [c,**]

[a] Center for Advanced Chemistry, Institute of Research and Development, Duy Tan University, Da Nang, 550000, Viet Nam
[b] Faculty of Natural Sciences, Duy Tan University, Da Nang, 550000, Viet Nam
[c] Division of Advanced Materials Engineering, Research Center for Advanced Materials Development, Jeonbuk National University, Jeonju, 54896, Republic of Korea
[d] National Nanofab Center, 291 Daehak-ro, Yuseong-gu, Daejeon, 34141, Republic of Korea
[e] Division of Liberal Art, Wonkwang University, Iksan, 54538, Republic of Korea

ARTICLE INFO

Keywords:
Core-shell structure NPs
Au nanorod core
ZnO shell
Visible-light activated
Hydrogen gas sensor

ABSTRACT

Au nanorods (NRs) in $Au_{nanorod}$@ZnO core-shell structure nanoparticles (CS-NPs) can improve the hydrogen gas sensing properties of ZnO NPs at room temperature under light irradiation in the visible to near-infrared region due to their tunable localized surface plasmon resonance (LSPR) along the transverse and longitudinal directions. In this study, the Au NR was first synthesized using a seed-mediated sequential growth process, followed by the deposition of a $Zn(OH)_2$ NP outer shell onto the Au NR core via a hydrothermal method. The $Au_{nanorod}$@$Zn(OH)_2$ CS-NPs were transformed into $Au_{nanorod}$@ZnO CS-NPs by calcination at 300°C for 5 h. The gas sensing characteristics of pure ZnO, $Au_{nanosphere}$@ZnO, and $Au_{nanorod}$@ZnO sensors were performed under visible light irradiation at different wavelengths using LEDs (i.e., blue light (450 nm), green light (515 nm), and red light (650 nm)) at room temperature. The hydrogen sensing responses of the $Au_{nanorod}$@ZnO sensor showed the highest values under blue, green, and red light irradiation, respectively, compared with pure ZnO and $Au_{nanosphere}$@ZnO, the highest hydrogen sensing response occurred under the red light. Notably, the $Au_{nanorod}$@ZnO sensor presents a high response of 6.26 towards 100 ppm hydrogen gas at room temperature under red light irradiation, which is about 5 times higher than its response to 100 ppm carbon monoxide. The enhanced gas sensing performance of the $Au_{nanorod}$@ZnO CS-NPs sensor could be attributed to the LSPR and electronic sensitization effects of the Au NRs core, along with the favorable structural and surface properties of the sensing material.

1. Introduction

Hydrogen gas has attracted public attention as one of the most promising renewable energy sources [1,2]. However, it also poses significant safety hazards, as many of the chemical properties that make it useful as an energy carrier are associated with extreme volatility. Hydrogen gas has a lower ignition energy (0.02 mJ) than other fuels, a high heat of combustion (142 kJ/g), and is flammable across a broad concentration range (4-75%) [3–8]. Consequently, the extensive efforts have been devoted to developing hydrogen gas sensors with the improved sensitivity, selectivity, stability, durability, energy efficiency, and safety [9–11].

The most common technologies used for gas sensing are based on electrochemical, catalytic, thermal conductivity, and various sensing materials, including metal oxides, MXenes, and metal sulfides [12–19]. Among these, metal oxide semiconductor (MOS) based chemiresistive gas sensors are considered one of the most promising hydrogen sensing technologies because of their simple device design and fabrication, low cost, good portability, high sensitivity, and excellent long-term stability [4,20–23]. The operation of chemiresistive gas sensors is based on changes in the electrical resistance (or conductivity) of semiconductor materials, which arise from a series of surface chemical processes, including the adsorption, reaction, and desorption of gas molecules [24–27]. In the case of hydrogen, a reducing gas, hydrogen molecules

* Corresponding author.
** Corresponding author.
E-mail addresses: oneday@wku.ac.kr (D.-H. Won), yeontae@jbnu.ac.kr (Y.-T. Yu).

https://doi.org/10.1016/j.mtnano.2026.100972
Received 17 July 2026; Received in revised form 13 September 2026; Accepted 1 October 2026
Available online 1 October 2026
2588-8420/© 2026 Elsevier Ltd. All rights are reserved, including those for text and data mining, AI training, and similar technologies.

react with chemisorbed oxygen species on the metal oxide surface, releasing electrons back to the semiconductor and thereby causing a measurable change in electrical resistance. Consequently, a variety of semiconducting metal oxides, such as SnO_2, ZnO, TiO_2, NiO, In_2O_3, MoO_3, and WO_3, have been extensively investigated as hydrogen sensing materials [28].

ZnO is an n-type MOS that has been extensively studied for hydrogen gas sensing due to its high sensitivity, simple synthesis, low cost, and good compatibility with sensor device fabrication process [29–32]. However, when operating at room temperature, the surface of ZnO is unable to provide sufficient activation energy, resulting in poor sensitivity and imperfect recovery in hydrogen detection [9,33–35]. To address these issues, several strategies have been proposed, including band gap modification of sensing materials [9,36,37], decoration with metal nanoparticles [38–48], and the use of photo-activatable materials [49–55]. Among them, photo-activatable materials are one of the best options, as they bypass the need for elevated temperature to activate the sensing reaction [53,54,56–60].

Accordingly, photo-activated Au nanorod-ZnO composite NPs can be proposed as a promising approach to improve the detection ability of hydrogen gas sensor operating at room temperature [9,34,35]. The introduction of Au nanorods (NRs) has been considered as an effective method to enhance the visible light absorption of ZnO materials, which can be attributed to the excitation of localized surface plasmon resonance (LSPR) effect along the transverse and longitudinal directions. The anisotropic morphology of Au NRs also provides wavelength dependent optical properties, and the longitudinal LSPR mode can generate a strong localized electromagnetic field under appropriate visible light excitation. In addition, the difference in work function between Au and ZnO can promote electron transfer at the Au/ZnO interface, resulting in electronic sensitization and modulation of the electrical properties of the ZnO sensing layer [59,61,62]. However, the Au NPs decorated on the surface of ZnO NPs tend to agglomerate at high operating temperatures [54,56,57,63–67]. To address this issue, a core-shell design may be more suitable for gas sensing applications, where the Au NR is encapsulated by a ZnO shell to form an $Au_{nanorod}$@ZnO CS-NP structure. Such a core-shell configuration can provide a stable Au/ZnO interface while combining the plasmonic and catalytic properties of Au with the gas sensing properties of ZnO.

In this research, the $Au_{nanorod}$@ZnO CS-NPs were synthesized by a hydrothermal method, and their gas sensing characteristics were evaluated under visible light irradiation at room temperature using LEDs with blue (450 nm), green (515 nm), and red (650 nm) wavelengths. Finally, by comparing with pure ZnO and $Au_{nanosphere}$@ZnO sensors, the hydrogen gas sensing mechanism of the $Au_{nanorod}$@ZnO CS-NPs sensor under photoactive conditions is clearly explained based on the LSPR effect of the Au NR core.

2. Experimental section

2.1. Chemicals

Hexadecyltrimethylammonium bromide (CTAB, $C_{19}H_{42}BrN$, 99%), ascorbic acid ($C_6H_8O_6$, 99%), silver nitrate ($AgNO_3$, 99.99%), zinc nitrate hexahydrate ($Zn(NO_3)_2.6H_2O$, 98%), and hexamethylenetetramine (HMTA, $C_6H_{12}N_4$, 99%) were supplied by Sigma Aldrich; sodium borohydride ($NaBH_4$, 98.5%) was bought from Showa Chemicals Co., Ltd.; and hydrogen tetrachloroaurate (III) hydrate ($HAuCl_4.3.7H_2O$, 99.99%) was purchased from Kojima Chemicals Co., Ltd.

2.2. Synthesis of Au NP seeds

In a typical synthesis method, 0.25 mL of an aqueous $HAuCl_4$ solution (10 mM) was mixed with 7.5 mL of an aqueous CTAB solution (100 mM) in a glass vial at 25°C. Next, 0.6 mL of an ice-cold aqueous $NaBH_4$ solution (10 mM) was rapidly added under stirring, and the mixture was stirred for 2 min, resulting in the formation of a brownish-yellow solution. The glass vial was then placed in a water bath maintained at 25°C. The seed solution was used 2 h after its preparation [68].

2.3. Synthesis of Au NRs

Au NRs were synthesized as follows. First, 0.8 mL of an aqueous $HAuCl_4$ solution (10 mM) and 0.12 mL of an aqueous $AgNO_3$ solution (10 mM) were added to 19 mL of an aqueous CTAB solution (100 mM) in a glass vial under gentle stirring at 25°C. The $AgNO_3$ was added as a shape-directing agent to promote the anisotropic growth of Au NRs. After 5 min of mixing, a bright brownish-yellow solution appeared. Next, 0.128 mL of an aqueous ascorbic acid solution (100 mM) was added. The solution became colorless upon the addition and mixing of ascorbic acid. Finally, 0.12 mL of the seed solution was injected into the mixture. The reaction mixture was gently mixed for 10 s and then placed in a water bath maintained at 25°C for 6 h. The product was collected by centrifugation at 10,000 rpm for 15 min and washed several times with distilled water and ethanol to remove surfactants. The collected Au NRs were redispersed in 5 mL of distilled water for later use [68].

2.4. Synthesis of $Au_{nanorod}$@ZnO CS-NPs

In the synthesis of $Au_{nanorod}$@ZnO CS-NPs, 4 mL of an aqueous CTAB solution (100 mM) was added to a 100 mL glass vial containing 50 mL of distilled water under vigorous stirring. Subsequently, 5 mL of the Au NRs colloid was added to the solution. Then, 1.0 mL of ascorbic acid (200 mM), 2 mL of $Zn(NO_3)_2.6H_2O$ (200 mM), and 2 mL of HMTA (200 mM) were introduced with continuous stirring for 10 min. Next, the glass vial was carefully sealed and heated at 86°C for 8 h in an oven.

After the reaction was completed, the $Au_{nanorod}$@$Zn(OH)_2$ CS-NPs were collected by centrifugation at 10,000 rpm for 15 min and washed several times with distilled water. The precipitated $Au_{nanorod}$@$Zn(OH)_2$ CS-NPs were dried at 60°C for 24 h. Finally, the dried powders were annealed in air at 300°C for 5 h to obtain $Au_{nanorod}$@ZnO CS-NPs [69]. ICP-OES analysis was performed to determine the Au/Zn molar ratios of the $Au_{nanorod}$@ZnO CS-NPs and $Au_{nanosphere}$@ZnO CS-NPs. The results are summarized in Table S1.

2.5. Characterization techniques

Transmission electron microscopy (TEM) images were obtained using a Cs-corrected transmission electron microscope (Cs-STEM) (JEOL, JEM-2010) operated at an accelerating voltage of 200 kV. UV-visible spectra were recorded at room temperature using a spectrophotometer (V-770, Jasco) in the wavelength range of 300–1000 nm. The crystal structure was analyzed by X-ray diffractometry (XRD; D/Max 2005, Rigaku) using CuK_α radiation ($\lambda = 1.54178$ Å) at 40 kV and 100 mA. The Au/Zn molar ratio was determined using an Inductively Coupled Plasma Optical Emission Spectrometer (ICP-OES, iCAP 7400 Duo, Thermo Fisher Scientific). The specific surface area and pore volume were measured using the Barrett-Emmett-Teller (BET) technique (Micromeritics TriStar 3000). The surface chemical states of the elements were analyzed by X-ray photoelectron spectroscopy (XPS) (Thermo Fisher Scientific, Multilab 2000) with a monochromated Al Kα X-ray source ($h\nu = 1486.6$ eV). Ultraviolet photoelectron spectroscopy (UPS) was performed using the same XPS system with a He I line – UV source (21.2 eV). The work function (Φ) was calculated from UPS spectra using the formula: $(\Phi) = E_{He\ I} - E_{cut\text{-}off}$ (eV) [69].

2.6. Fabrication and measurement of gas sensing device

To fabricate the sensor devices, gold wires were first connected to the Pt interdigitated electrodes on an alumina circuit board (Ogam Technology Co. Ltd, electrode area = 10 mm × 10 mm) using gold paste. The assembled circuit boards were then sintered at 500°C for 2 h with a

heating rate of 1 °C/min to remove residual organic components. After cooling, the edges of each circuit board were masked with adhesive tape to define the sensing area. Subsequently, 20 mg of the sensing material was thoroughly mixed with 10 μL of α-terpineol in a mortar to form a homogeneous paste. The resulting paste was uniformly coated onto the electrode area (10 mm × 10 mm) of the alumina circuit board to form the sensing film. Before gas sensing measurements, the fabricated devices were dried overnight at 60°C and subsequently annealed at 300°C for 5 h with a heating rate of 1° C/min in a muffle furnace to remove residual solvent and improve the adhesion of the sensing layer (Fig. S1). As shown in Fig. S2, the Au nanorod morphology and ZnO shell structure were well preserved after this additional annealing step, indicating that the heat treatment did not induce any noticeable structural changes.

The sensing test system consists of three parts: gas supply, LED light sources, and electric resistance signal detection. The gas sensing properties of the prepared devices were investigated at room temperature (~20°C) under visible light illumination with different wavelengths using LEDs (9.8 W) emitting blue (450 nm), green (515 nm), and red (650 nm) light. The sensor device is placed at the inner center of a quartz test tube during the photoactivated measurements, and LED lights are placed on the outer center of the quartz tube. The actual distance between the LED light and the sensing device is 2.5 cm (Fig. S3). The experimental geometry and LED–sensor distance were kept identical throughout all measurements, with the LED wavelength being the only experimental variable. The sensor device was enclosed inside the quartz tube during the sensing measurements. Therefore, the sensor surface temperature under LED illumination was not directly measured in the present study. A 200 ppm H_2 gas mixture balanced with N_2 was purchased from Hankook Special Gases Co., Ltd. (Republic of Korea). The target gases, including hydrogen (H_2), acetaldehyde (CH_3CHO), ethanol (C_2H_5OH), methane (CH_4), and carbon monoxide (CO), were introduced into a high dynamic reaction chamber at different concentrations ranging from 1 to 100 ppm, with nitrogen (N_2) as the balance gas. Meanwhile, the N_2 was used as the background gas and dry air (21% O_2) was mixed to maintain an oxygen (O_2) concentration of 10.5%. The total gas flow rate was kept at 100 sccm using a mass flow controller (MFC) by computer management, and the oxygen content was constantly maintained at 10.5% to ensure a consistent and reproducible sensing atmosphere for evaluating the sensor performance. The effect of humidity on the hydrogen sensing performance of the sensor was systematically investigated. Humid air was generated by bubbling dry air through deionized water, with the relative humidity (RH%) controlled at 20%, 40%, 60%, and 80% by adjusting the air flow rate. To ensure accurate humidity control, a hygrometer was positioned immediately upstream of the sensing chamber to monitor the RH% before the gas mixture entered the chamber (Fig. S3). A high resistance meter (Agilent 34970A) recorded the sensor's resistance changes during gas testing. The gas sensing response (S) toward reducing gases was calculated as R_a/R_g, where R_a was the sensor resistance in dry air and R_g was the resistance in the presence of the target gas [9,67,69].

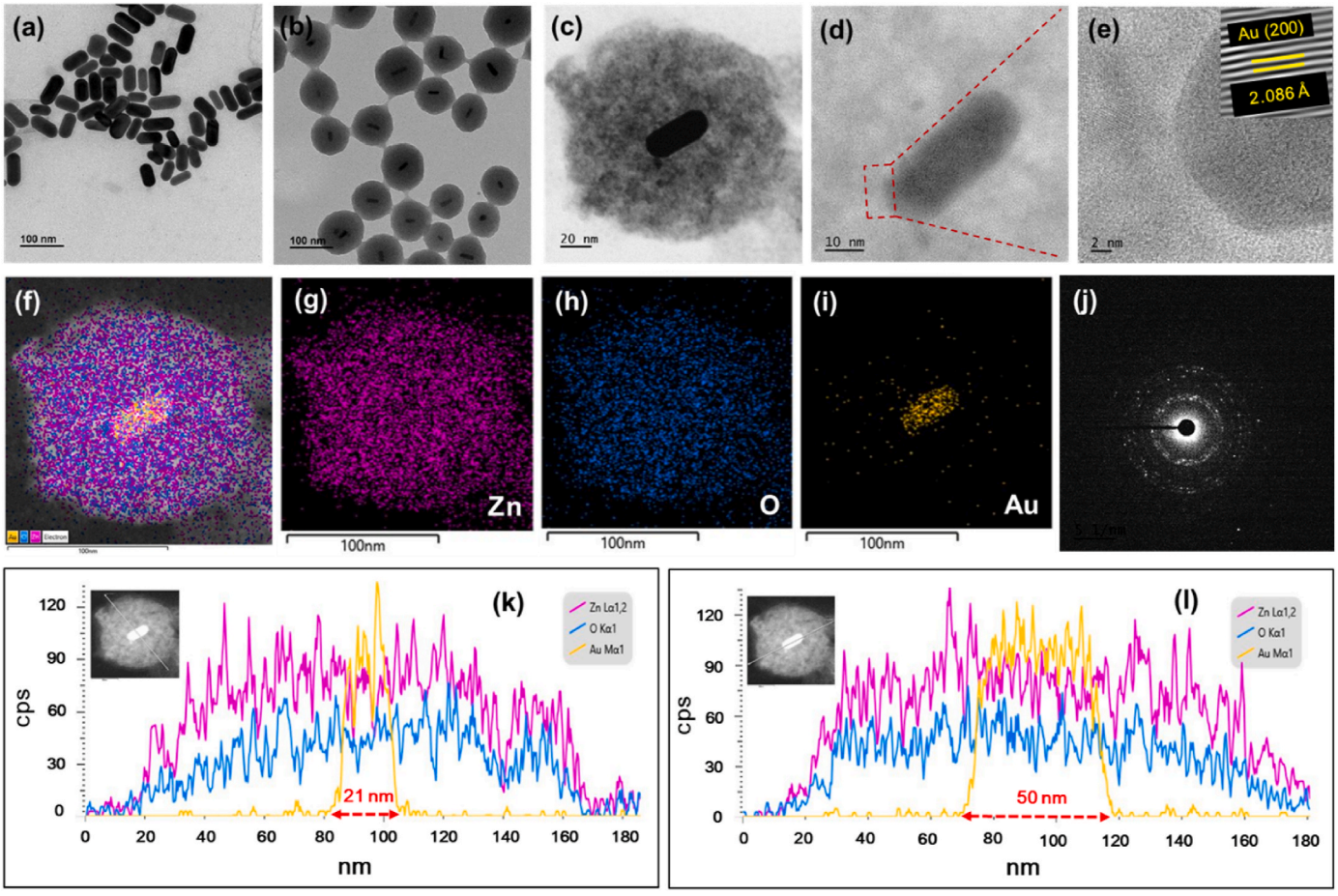


Fig. 1. TEM and HAADF-STEM images of (a) Au NRs, (b) $Au_{nanorod}@Zn(OH)_2$ CS-NPs, (c) $Au_{nanorod}@ZnO$ CS-NPs, (d) high magnification of $Au_{nanorod}@ZnO$ CS-NPs, (e) lattice fringe of the Au nanorod. (f-i) STEM-EDS results of $Au_{nanorod}@ZnO$ CS-NPs with elemental maps for their overlay (f); Zn (g); O (h); Au (i). (j) corresponding SAED pattern of $Au_{nanorod}@ZnO$ CS-NPs. (k and l) corresponding EDS line scanning profiles of Au (yellow); Zn (pink) and O (blue) along transverse (k) and longitudinal (l) directions of Au nanorod core in $Au_{nanorod}@ZnO$ CS-NPs. The x-axis represents the distance along the line scan (nm) and the y-axis refers to the number of counts (counts per second, cps).

3. Results and discussion

3.1. Material characterizations

The morphology of materials was observed using transmission electron microscopy (TEM). Fig. 1a presented the TEM image of Au NRs with a uniform length and width of 45–55 nm and 18–23 nm, respectively. Fig. S4 supported the TEM analysis of pure $Zn(OH)_2$ NPs with an average size of about 90 nm. The as-prepared $Au_{nanorod}$@$Zn(OH)_2$ CS-NPs were as shown in Fig. 1b, they exhibited very smooth surfaces due to the existence of the CTAB surfactant. They consisted of an Au NR core and a $Zn(OH)_2$ shell with an average diameter of about 100 nm. After calcination at 300°C, the $Au_{nanorod}$@$Zn(OH)_2$ CS-NPs were transformed into $Au_{nanorod}$@ZnO CS-NPs due to the crystallization of tiny ZnO NPs (Fig. 1c). The thickness of the ZnO shell in the $Au_{nanorod}$@ZnO CS-NPs was determined to be around 60 nm. The single crystalline nature of these $Au_{nanorod}$@ZnO CS-NPs was confirmed by high-resolution TEM (HR-TEM) as shown in Fig. 1d and e. The lattice spacing of 2.086 Å corresponds to the (200) plane of Au, indicating that the Au NRs preferentially grew along the [200] direction. Besides, the TEM elemental mapping of the $Au_{nanorod}$@ZnO CS-NPs was presented in Fig. 1f–j. The pink area of the Zn and blue area of the O surrounded the yellow area of the Au, reflecting the core-shell structure. In addition, the selected area electron diffraction (SAED) pattern showed a ring pattern, which confirmed the crystalline structure of the $Au_{nanorod}$@ZnO CS-NPs (Fig. 1j). Moreover, the corresponding EDS line scanning profiles for Au (yellow), Zn (pink), and O (blue) of the $Au_{nanorod}$@ZnO CS-NPs along transverse and longitudinal directions indicated that the $Au_{nanorod}$@ZnO core-shell structure was stable after calcination at 300°C (Fig. 1k and l). These results showed that the Au NR core was about 21 nm in diameter and 50 nm in length. To compare with the $Au_{nanorod}$@ZnO CS-NPs, $Au_{nanosphere}$@ZnO CS-NPs were also prepared. Notably, the Au NS core had a lattice spacing of 2.301 Å corresponding to the (111) crystal plane and its particle size of about 30 nm (Fig. S5 and S6).

The optical properties of all materials were characterized using UV-visible absorption spectroscopy (Fig. 2a). The surface plasmon resonance (SPR) effect depends on the dipole moment of the nanoparticles, which is influenced by various factors such as size, shape, material composition, surface coating, and surrounding medium. In the case of Au NRs, they had two SPR wavelengths. The first SPR peak at 528 nm was due to the transverse mode perpendicular to the Au NRs, and the second SPR peak at 786 nm was due to the length of the Au NRs which gave rise to the longitudinal mode of SPR with a higher peak. It is noteworthy that the two characteristic peaks of Au NR exhibited shifted to 531 nm (transverse mode) and to 638 nm (longitudinal mode) in the absorption peak of $Au_{nanorod}$@ZnO CS-NPs. This is due to the larger refractive index of ZnO encapsulating the Au cores. The ZnO characteristic absorption peak for $Au_{nanorod}$@ZnO CS-NPs was observed at 378 nm. Meanwhile, the SPR peak of the Au NSs was initially recorded at 527 nm and red-shifted to 557 nm following ZnO shell formation (Table S2).

XRD study was performed to investigate the crystal structure of the prepared materials, including Au NRs, Au NSs, as-calcined pure ZnO NPs, $Au_{nanorod}$@ZnO CS-NPs, and $Au_{nanosphere}$@ZnO CS-NPs (Fig. 2b and c). The XRD main peaks of the Au NRs were observable at 38.08°, 44.28°, and 64.52° corresponding to the (111), (200), and (220) planes. The XRD profile of the Au NRs showed a strong (111) diffraction peak, and the intensity of the (200) diffraction peak was also strong. The enhanced (200) diffraction confirmed that the elongation of Au NRs facet mainly accounted for the crystal growth. Meanwhile, the XRD peaks of the Au NSs were apparent at 37.98°, 44.18°, and 64.5° corresponding to the (111), (200), and (220) planes (Fig. 2b). Notably, the peak at 37.98° was a main peak of Au NSs which the growth rate along the (111) direction was much higher than those of (200) and (220) direction. Furthermore, the XRD diffraction pattern of as-prepared core-shell heterostructures showed strong ZnO diffraction peaks and weak diffraction peaks of metallic Au NRs in $Au_{nanorod}$@ZnO CS-NPs and Au NSs in $Au_{nanosphere}$@ZnO CS-NPs. The remained ZnO peaks in both specimens were indexed to be wurtzite structure (JCPDS No.36-1451) (Fig. 2c).

Fig. S7 and 3 showed XPS spectra characterization of ZnO NPs, $Au_{nanosphere}$@ZnO CS-NPs, and $Au_{nanorod}$@ZnO CS-NPs. In the survey spectra of the Au@ZnO CS-NPs (Fig. S7), all elements, namely, Zn, O and Au, were detected with strong characteristic peaks. Fig. 3a presented the

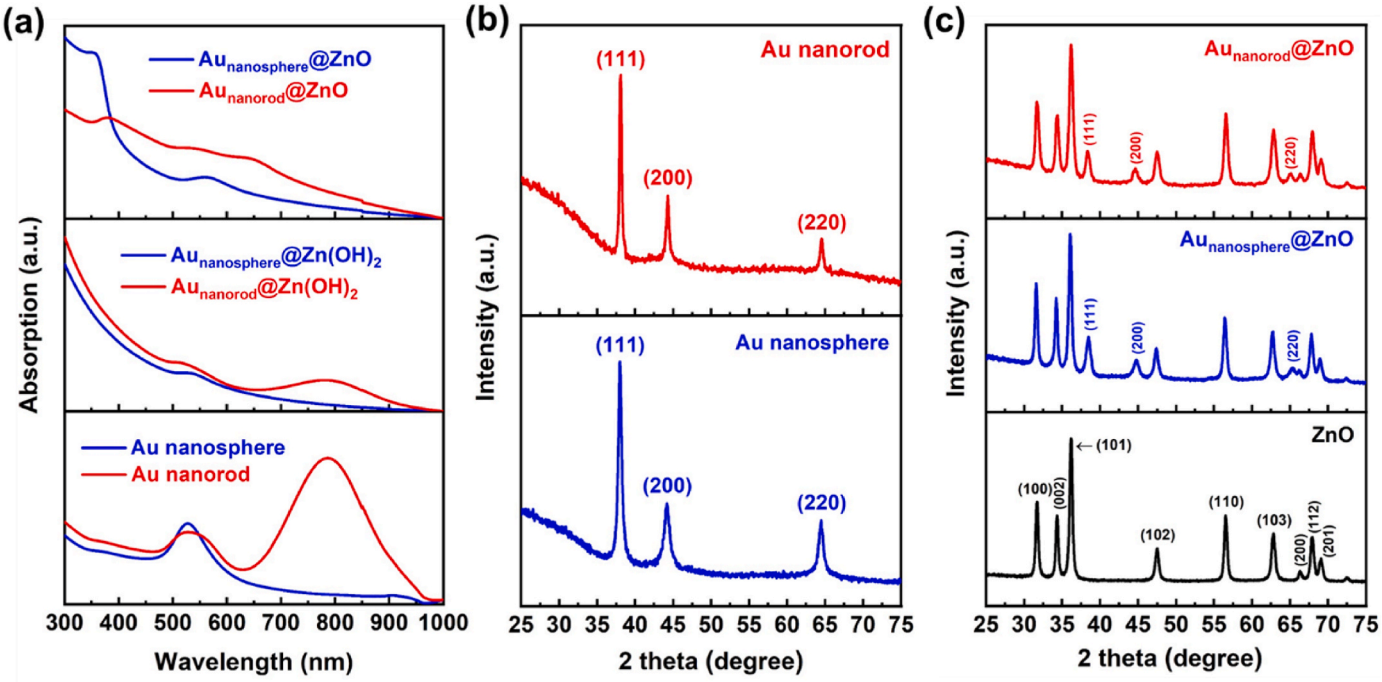


Fig. 2. (a) UV-visible absorption spectra of Au nanosphere and Au nanorod, $Au_{nanosphere}$@$Zn(OH)_2$ CS-NPs and $Au_{nanorod}$@$Zn(OH)_2$ CS-NPs, and $Au_{nanosphere}$@ZnO CS-NPs and $Au_{nanorod}$@ZnO CS-NPs. XRD patterns of (b) Au nanosphere and Au nanorod, and (c) ZnO NPs, $Au_{nanosphere}$@ZnO CS-NPs and $Au_{nanorod}$@ZnO CS-NPs.

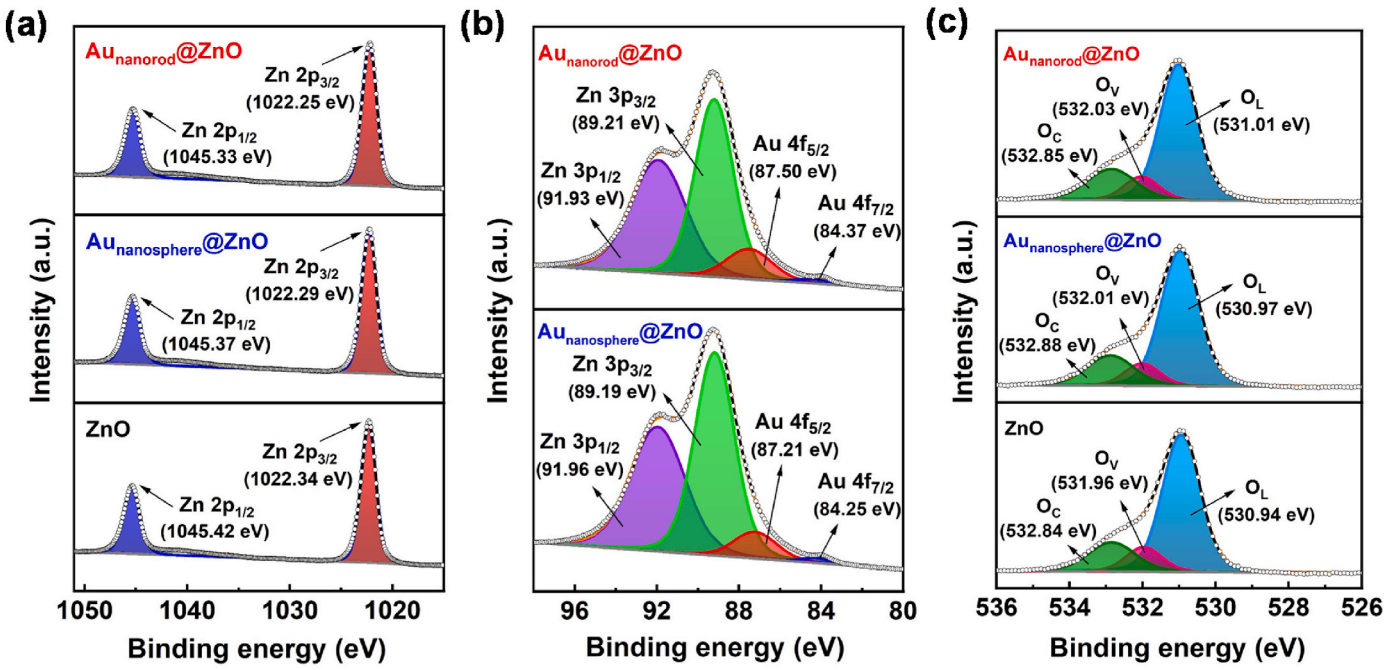


Fig. 3. XPS survey spectrum of (a) Zn 2p, (b) Zn 3p–Au 4f, and (c) O 1s of ZnO NPs, $Au_{nanosphere}$@ZnO CS-NPs, and $Au_{nanorod}$@ZnO CS-NPs.

two main peaks of Zn 2p at 1045.42 eV ($2p_{1/2}$) and 1022.34 eV ($2p_{3/2}$) with an inter-peak distance of 23.08 eV, indicating the existence of Zn^{2+} oxidation state (ZnO) in the material. Meanwhile, the Zn 2p XPS spectra of Au@ZnO CS-NPs recorded at 1045.37 eV and 1022.29 eV for $Au_{nanosphere}$@ZnO CS-NPs, and at 1045.33 eV and 1022.25 eV for $Au_{nanorod}$@ZnO CS-NPs. A red shift to a lower binding energy value with the introduction of Au NPs occurred due to the strong exchange of electron between the ZnO shell and Au core [70–72]. The deconvolution confirmed the presence of four distinct peaks assigned to the double peak features of Zn $3p_{3/2}$ and Zn $3p_{1/2}$ for Zn 3p and Au $4f_{7/2}$ and Au $4f_{5/2}$ for Au 4f (Fig. 3b). In $Au_{nanorod}$@ZnO CS-NPs, the two peaks located at 89.21 eV (Zn $3p_{3/2}$) and 91.93 eV (Zn $3p_{1/2}$) of Zn^{2+} cations. The other two peaks had binding energies of 87.50 eV (Au $4f_{5/2}$) and 84.37 eV (Au $4f_{7/2}$) of $Au^{\delta+}$ [73–75]. The binding energy peak position of Au 4f in $Au_{nanorod}$@ZnO CS-NPs was blue-shifted towards higher values compared to $Au_{nanosphere}$@ZnO CS-NPs (Au $4f_{5/2}$, 87.21 eV and Au $4f_{7/2}$, 84.25 eV). This result revealed that more electrons were moved from the ZnO shell to the Au nanorod core than to the Au nanosphere core. Also, the percentages of Zn 3p and Au 4f in $Au_{nanosphere}$@ZnO CS-NPs and $Au_{nanorod}$@ZnO CS-NPs were summarized in Table S3. The O 1s peaks were fitted into three peaks located at 530.94, 531.96, and 532.84 eV as shown in Fig. 3c, indicating three different kinds of oxygen species in ZnO NPs. The oxygen peak at 530.94 eV was ascribed to lattice oxygen (O_L) in the wurtzite structure that was surrounded by zinc atoms that had their full complement of nearest-neighbor O^{2-} ions. The medium oxygen peak at 531.96 eV was ascribed to O^{2-} ions in oxygen vacancy (O_V) regions within the ZnO matrix. The oxygen peak at 532.84 eV was attributed to chemisorbed oxygen (O_C) caused by the ZnO surface. The relative percentages of O_L, O_V, and O_C components were about 70.86%, 10.75%, and 18.39% in the ZnO material. With the introduction of Au NPs, the proportions of oxygen vacancy and chemisorbed oxygen species were increased. The contents of O_V and O_C were 11.14% and 19.22% for $Au_{nanosphere}$@ZnO CS-NPs and 11.96% and 20.32% for $Au_{nanorod}$@ZnO CS-NPs (Table S4). Therefore, Au NRs enhanced the oxygen chemisorbed ability of ZnO, which can greatly contribute to the gas sensing properties of surface resistance-type metal oxide semiconductors.

The specific surface area and pore size distribution of the materials were characterized by nitrogen adsorption-desorption measurements (Fig. 4 and S8). All samples exhibited a type IV isotherm, reflecting the

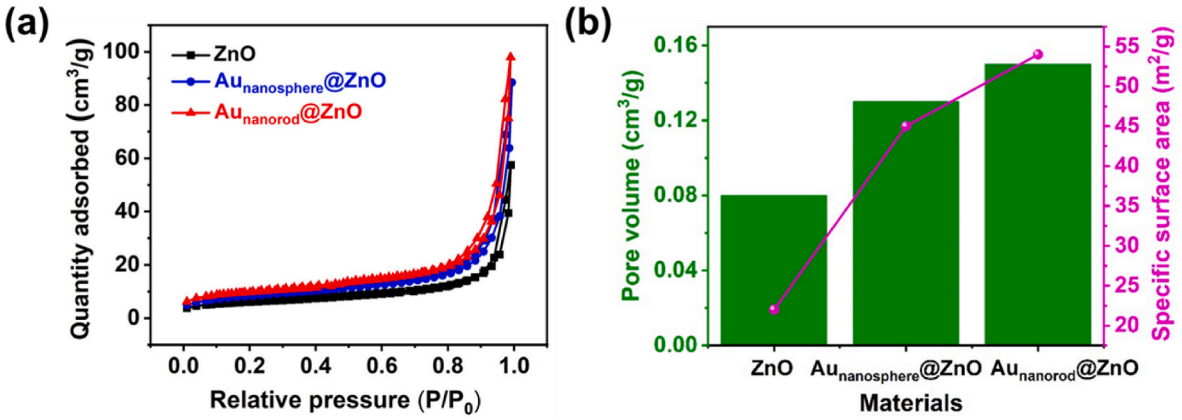


Fig. 4. (a) Nitrogen adsorption/desorption isotherm measurements and (b) corresponding pore volume and specific surface area for pure ZnO, $Au_{nanosphere}$@ZnO CS-NPs, and $Au_{nanorod}$@ZnO CS-NPs.

presence of mesopores. Based on the BET analysis results, the specific surface areas of ZnO NPs, $Au_{nanosphere}$@ZnO CS-NPs, and $Au_{nanorod}$@ZnO CS-NPs were calculated to be 22, 45, and 54 m^2/g, respectively (Table S5). These results demonstrated that the specific surface area of ZnO NPs increased dramatically after forming the $Au_{nanorod}$@ZnO core-shell structure. In addition, the N_2 absorption capacity of the $Au_{nanorod}$@ZnO CS-NPs was higher than that of both the $Au_{nanosphere}$@ZnO CS-NPs and pure ZnO NPs, indicating the pore volume of $Au_{nanorod}$@ZnO CS-NPs (0.15 cm^3/g) was higher than $Au_{nanosphere}$@ZnO CS-NPs (0.13 cm^3/g) and ZnO NPs (0.08 cm^3/g) (Table S5). Among the samples, the $Au_{nanorod}$@ZnO CS-NPs possessed the highest specific surface area and pore volume. Consequently, their surface contains more active sites for oxygen adsorption on the surface of materials and is expected to have better gas sensing properties.

3.2. Gas sensing performances

To investigate the sensitivity of the pure ZnO, $Au_{nanosphere}$@ZnO, and $Au_{nanorod}$@ZnO sensors towards reducing gases (i.e., H_2), different concentrations of hydrogen (10–100 ppm) were applied to the chamber under LED lights with different wavelengths (nm), including blue light (450 nm), green light (515 nm), and red light (650 nm). All sensors exhibited the typical n-type semiconducting behaviors with a decrease in resistance after the expose of target gas. Fig. 5 showed the hydrogen gas sensing activity to 100 ppm hydrogen at room temperature under the illumination of blue, green, and red lights of pure ZnO, $Au_{nanosphere}$@ZnO, and $Au_{nanorod}$@ZnO sensors. For the sensors exposed to hydrogen with different concentrations, the increased resistance in air was the most significant under 450 nm blue light activation for the pure ZnO sensor, 515 nm green light activation for the $Au_{nanosphere}$@ZnO sensor, and 650 nm red light activation for the $Au_{nanorod}$@ZnO sensor. Particularly, the R_a of pure ZnO, $Au_{nanosphere}$@ZnO, and $Au_{nanorod}$@ZnO sensors towards 100 ppm hydrogen was 5.01 kΩ (blue light), 23.91 kΩ (green light), and 49.28 kΩ (red light), respectively (Fig. 5a–c). The slight upward drift in the baseline resistance (R_a) during successive sensing cycles is attributed to the relatively slow re-adsorption of oxygen species after exposure to H_2 under continuous LED illumination at room temperature. Consequently, the baseline resistance does not completely recover to the identical initial state before the subsequent sensing cycle, resulting in a gradual increase in R_a (Fig. 5a–c). The gas responses of pure ZnO, $Au_{nanosphere}$@ZnO, and $Au_{nanorod}$@ZnO sensors were presented in Fig. 5d. With the absence of Au NPs, the hydrogen responses of the pure ZnO were low, including $S_{blue} = 1.10$, $S_{green} = 1.05$, and $S_{red} = 1.02$. The response values of the $Au_{nanosphere}$@ZnO sensor were slightly higher such as $S_{green} = 2.56$, $S_{red} = 1.39$, and $S_{blue} = 1.12$. Because the LSPR absorption peak of the $Au_{nanosphere}$@ZnO CS-NPs is centered at 557 nm, which is closer to the wavelength of the green LED (515 nm), green light irradiation induces a larger decrease in R_g, resulting in the highest sensing response. Notably, the $Au_{nanorod}$@ZnO sensor showed an excellent response ($S_{red} = 6.26$, $S_{green} = 3.29$, and $S_{blue} = 1.39$) to 100 ppm hydrogen gas at room temperature. Therefore, the operation of the pure ZnO, $Au_{nanosphere}$@ZnO, and $Au_{nanorod}$@ZnO sensors corresponding to blue, green, and red light was considered as their optimal condition. This result happened due to the presence of the LSPR effect by Au NRs (transverse and longitudinal modes) in the $Au_{nanorod}$@ZnO sensor enhanced the absorption in the visible light range (i.e., red light) providing sufficient energy to promote the sensor response compared to pure ZnO and $Au_{nanosphere}$@ZnO sensors. In addition, Fig. S9 showed the transient resistance curve of the $Au_{nanorod}$@ZnO sensor toward 100 ppm hydrogen at room temperature under

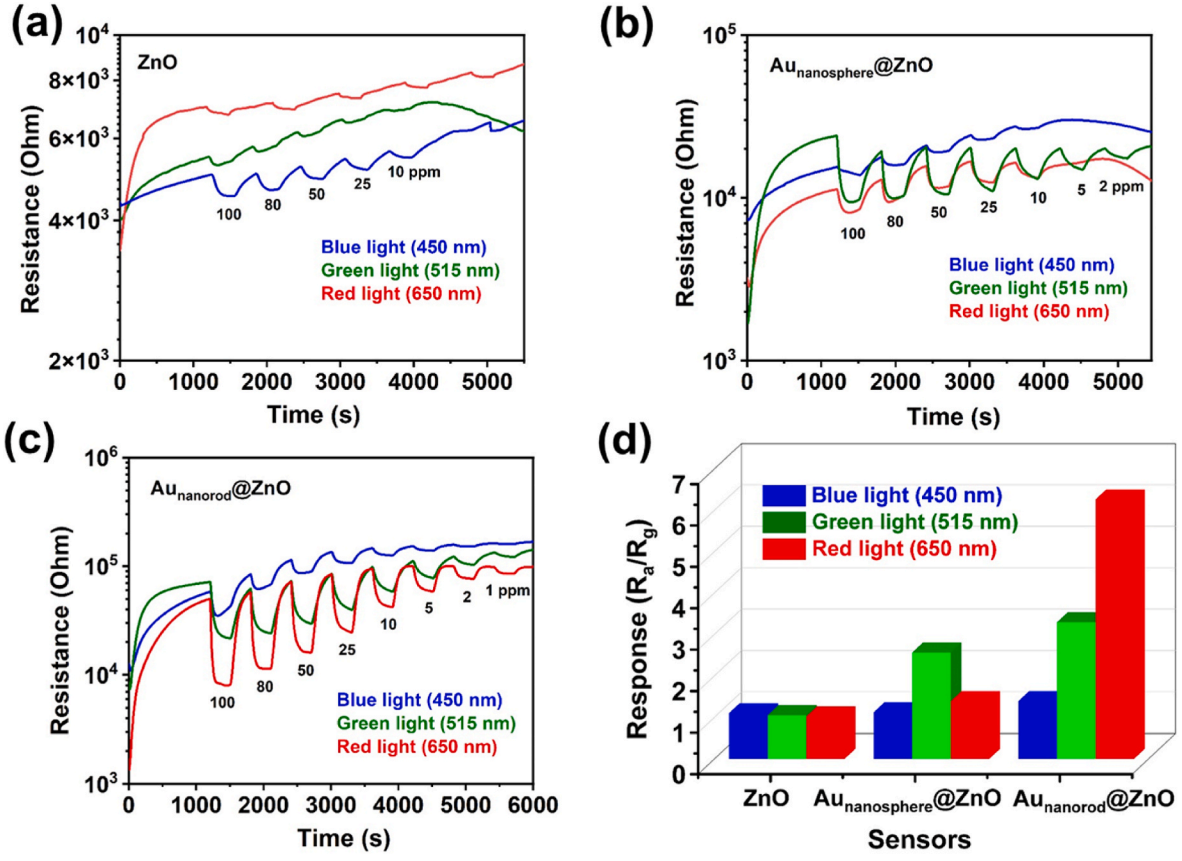


Fig. 5. Gas sensing activity to 100 ppm hydrogen at room temperature under the illumination of blue, green, and red lights of (a) ZnO sensor, (b) $Au_{nanosphere}$@ZnO sensor, and (c) $Au_{nanorod}$@ZnO sensor. (d) Gas responses of ZnO, $Au_{nanosphere}$@ZnO, and $Au_{nanorod}$@ZnO sensors to 100 ppm hydrogen at room temperature under the illuminations.

LED lights. The resistance decreases upon exposure to H_2, which is the typical sensing behavior of an n-type ZnO-based semiconductor sensor. Under resonant LED illumination, the LSPR of the Au NRs further enhances charge transfer and accelerates the reaction between H_2 molecules and chemisorbed oxygen species, leading to a substantial decrease in the resistance in the presence of H_2 (R_g). The sensing response of an n-type semiconductor sensor is determined by the ratio $S = R_a/R_g$. The electrical resistance of this sensor decreased upon exposure to hydrogen gas under LED illumination and increased upon exposure to dry air. Consequently, the sensing response is significantly enhanced. The electrical resistance of the $Au_{nanorod}$@ZnO sensor in dry air and hydrogen gas under LED lights was summarized in Table S6. For the $Au_{nanorod}$@ZnO sensor, R_a under red light irradiation (49,280 Ω) was lower than that under green light irradiation (71,101 Ω), whereas R_g decreased much more markedly from 21,611 Ω to 7872 Ω. As a result, the R_a/R_g ratio increased from 3.29 to 6.26, giving the highest sensing response under red light irradiation. Moreover, the transient resistance curve change of the $Au_{nanorod}$@ZnO sensor at room temperature when dry air, red light, and hydrogen gas were applied, respectively was presented in Fig. S10. Before introducing the LED illumination (e.g., red light) and hydrogen gas, the baseline electrical resistance of the $Au_{nanorod}$@ZnO sensor increased in the dry air environment. Then, the electrical resistance of this sensor decreased under LED light irradiation. Next, 100 ppm of hydrogen was introduced into the chamber, the electrical resistance of this sensor continued to reduce and was then recovered by reintroducing dry air (Fig. S10). The change in electrical resistance of $Au_{nanorod}$@ZnO CS-NPs under red light is related to the LSPR effect of the Au nanorod core. These CS-NPs exhibit a strong absorption peak at 638 nm, close to the 650 nm wavelength of the red LED (Fig. 2a). This resonance enables localized surface electrons to transfer from the Au nanorod core to ZnO shell, thereby reducing the electrical resistance of the $Au_{nanorod}$@ZnO CS-NPs.

Fig. 6a showed the hydrogen gas concentration versus response graph of all sensors such as pure ZnO, $Au_{nanosphere}$@ZnO, and $Au_{nanorod}$@ZnO sensors measured at room temperature using their optimal LED light condition. As the hydrogen concentration increased from low to high, the responses of pure ZnO, $Au_{nanosphere}$@ZnO, and $Au_{nanorod}$@ZnO sensors increased. Among the tested sensors, the response values of the $Au_{nanorod}$@ZnO sensor increased rapidly from 2.25 to 6.26 in the hydrogen concentration range of 10–100 ppm under red light illumination. In addition, the $Au_{nanorod}$@ZnO sensor exhibited a response value of 1.16 to 1 ppm H_2, the lowest hydrogen concentration tested in this study, under red light illumination at room temperature (Table S7). The response and recovery times were considered as important parameters for any gas sensing devices. The response time was defined as the time taken by the sensor to achieve 90% of the total resistance change during target gas adsorption, while recovery time was denoted as the time at 90% of resistance change during target gas desorption by the supply of air. The response and recovery times of the ZnO, $Au_{nanosphere}$@ZnO, and $Au_{nanorod}$@ZnO sensors towards 100 ppm hydrogen at room temperature under different light irradiation wavelengths were shown in Fig. 6b–S11 and Table S8. For the ZnO sensor, the response times under red, green, and blue light were 300, 100, and 180 s, respectively, while the corresponding recovery times were 490, 310, and 330 s. After the introduction of Au nanospheres, the $Au_{nanosphere}$@ZnO sensor exhibited faster response times of 90, 80, and 110 s and recovery times of 250, 240, and 280 s under red, green, and blue light, respectively. Notably, the $Au_{nanorod}$@ZnO sensor exhibited the shortest response and recovery times among the three sensors. Its response and recovery times under red, green, and blue light were 50 and 190 s, 60 and 220 s, and 100 and 260 s, respectively. In particular, the shortest response and recovery times were obtained under red light irradiation. This can be attributed to the efficient excitation of the longitudinal LSPR of the Au NRs, whose absorption peak is centered at approximately 638 nm. Because this wavelength closely matches that of the red LED (650 nm), the longitudinal LSPR is excited more efficiently under red light than under blue or green light irradiation, thereby enhancing charge transfer and accelerating the reaction between H_2 molecules and chemisorbed oxygen species on the ZnO surface. In addition, the enhanced charge transfer may facilitate oxygen re-adsorption onto the ZnO surface after

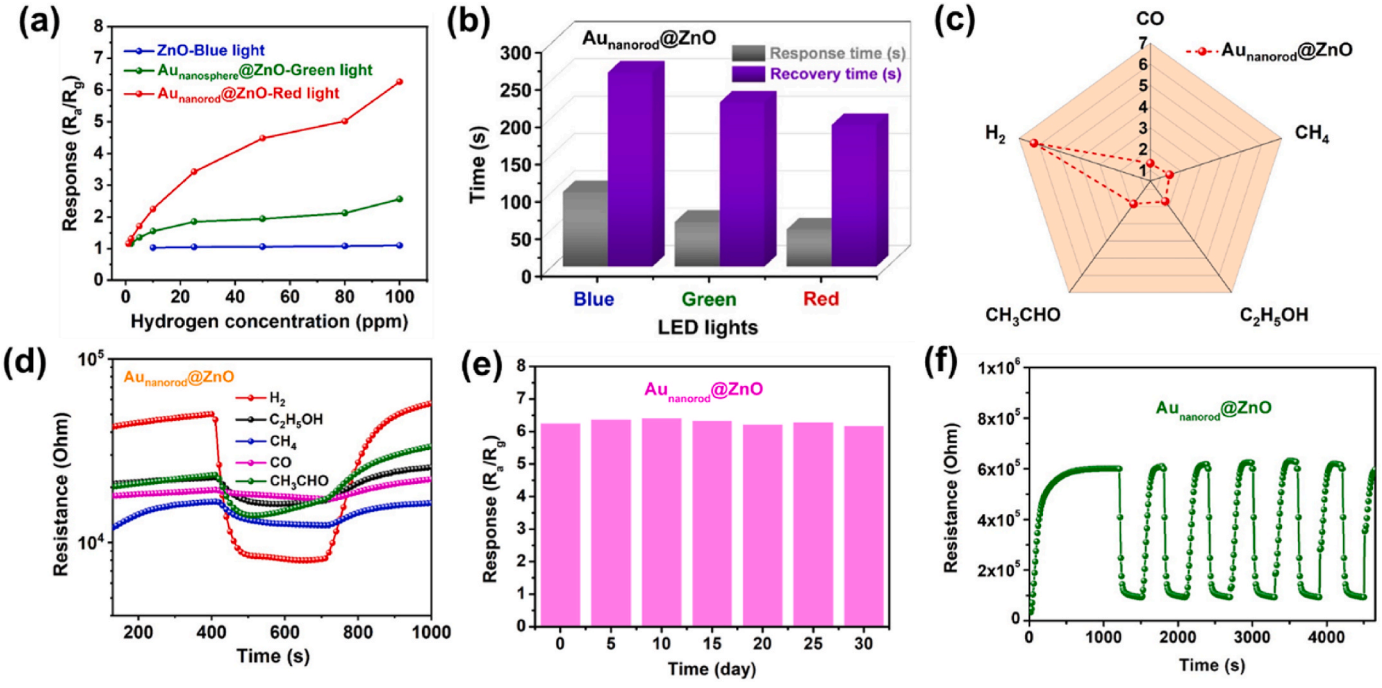


Fig. 6. (a) Sensing response in the range of 10–100 ppm hydrogen for all sensors, (b) response and recovery properties to 100 ppm hydrogen for $Au_{nanorod}$@ZnO sensor at room temperature under the illuminations, (c) selectivity test with 100 ppm of different target gases for $Au_{nanorod}$@ZnO sensor at room temperature under red light, (d) resistance change of the $Au_{nanorod}$@ZnO sensor to 100 ppm of various target at room temperature under LED lights, (e) long-term stability of gas sensors in 100 ppm hydrogen for 30 days, and (f) 6 cycles of transient response-recovery curves of the $Au_{nanorod}$@ZnO sensor to 100 ppm of hydrogen.

H_2 is removed, contributing to faster recovery. Consequently, the $Au_{nanorod}$@ZnO sensor exhibits shorter response and recovery times under red light irradiation than under blue or green light irradiation. The gas selectivity of the $Au_{nanorod}$@ZnO sensor was evaluated under red light irradiation at room temperature, which was selected as the optimum operating condition based on its highest H_2 sensing response (Fig. 6c and d). The response was assessed by testing with other interfering gases such as hydrogen (H_2), acetaldehyde (CH_3CHO), ethanol (C_2H_5OH), methane (CH_4), and carbon monoxide (CO) with a concentration of 100 ppm at room temperature. The $Au_{nanorod}$@ZnO sensor exhibited high selectivity to H_2 among other interfering gases indicating that this sensor had a better ability to discriminate H_2 gas. In particular, the $Au_{nanorod}$@ZnO sensor's response was 1.33 for CO, 1.45 for CH_4, 1.69 for C_2H_5OH, 1.84 for CH_3CHO, and 6.26 for H_2 (Table S9). Moreover, the $Au_{nanorod}$@ZnO sensor was tested under LED lights with different power consumptions in the watt (W), including 2.1 W and 4.9 W (Fig. S12). The $Au_{nanorod}$@ZnO sensor demonstrated a higher response, corresponding to higher power consumption. Although the sensing response increased with increasing LED power, this behavior alone does not necessarily indicate that photothermal heating is the dominant mechanism. Because the sensing device is placed at the inner center of a quartz tube and LED lights are placed on the outer center of the tube. Increasing the LED power also increases the incident optical intensity and consequently enhances the optical excitation of the Au nanorods, which can strengthen the LSPR mediated photoactivation of the $Au_{nanorod}$@ZnO sensing layer. Among the tested LED lights, the $Au_{nanorod}$@ZnO sensor showed an excellent response to 100 ppm hydrogen at room temperature under red light, compared to blue and green light (Fig. 5, S12, and Table S10). The long-term stability of the $Au_{nanorod}$@ZnO sensor was evaluated over a 30-day storage period, as shown in Fig. 6e. During this period, the sensing response showed only a slight decrease from an initial value of 6.26 to 6.18 after 30 days, indicating excellent long-term stability. The repeatability of the $Au_{nanorod}$@ZnO sensor was further evaluated at room temperature under red light illumination (Fig. 6f). Six consecutive sensing cycles were conducted using 100 ppm hydrogen, and the sensor exhibited nearly identical response-recovery characteristics throughout the repeated air/hydrogen switching process, demonstrating excellent repeatability and stable sensing performance. Furthermore, the additional gas sensing tests were performed for other interfering gases, including NO_2 and H_2S, as shown in Fig. S13. The responses of the $Au_{nanorod}$@ZnO CS-NPs sensor toward 100 ppm NO_2 and H_2S at room temperature under red light illumination (9.8 W) were 1.52 and 1.78, respectively.

Moreover, the effect of humidity on the hydrogen sensing performance of the sensor was systematically investigated. As shown in Fig. S14 and Table S11, the response of the $Au_{nanorod}$@ZnO sensor to 100 ppm H_2 under red light illumination (9.8 W) at room temperature decreased from 5.02 at 20% RH to 3.30, 1.66, and 1.39 at 40%, 60%, and 80% RH, respectively. The decrease in response is attributed to the competitive adsorption of water molecules and the formation of surface hydroxyl groups, which reduce the amount of chemisorbed oxygen species available for reaction with hydrogen. Despite the considerable humidity induced decrease in response, the sensor remained capable of detecting 100 ppm H_2 even at 80% RH under room temperature operation, although humidity clearly had a significant influence on its sensing performance. Furthermore, Table S12 compares the hydrogen sensing performance of the $Au_{nanorod}$@ZnO CS-NPs sensor in the present study with those of sensors reported in previous studies.

3.3. Gas sensing mechanism

The UV-visible absorption peak of $Au_{nanorod}$@ZnO CS-NPs was strong at 638 nm (Fig. 2a and Table S2). This peak wavelength closely matched the wavelength (650 nm) of the red LED used in this study. As a result, the $Au_{nanorod}$@ZnO CS-NPs sensor exhibited great hydrogen gas sensing performances at room temperature under red light (650 nm) compared to green (515 nm) and blue (450 nm) lights (Fig. 5c and d). Therefore, the gas sensing mechanism was explained based on the change in electrical resistance of the n-type MOS sensor tested at room temperature under red light condition. In the air, the ZnO sensing surface attracted oxygen molecules (O_2) by chemisorption, which increased the width of electron depletion layer as well as baseline resistance of this sensor due to form chemisorbed oxygen anions (O_2^-) (Eq. (1)). Under LED light irradiation, the photoexcited electrons ($e^-_{(h\nu)}$) and holes (h^+) were generated (Eq. (2)). Followed by, the photo-induced oxygen anions ($O^-_{2(h\nu)}$) is formed on a highly active surface of ZnO (Eq. (3)). When the sensor exposed to the hydrogen gas, the electrical resistance and the electron depletion layer were decreased. This phenomenon was related to the chemical reaction of hydrogen molecules (H_2) with the chemisorbed oxygen anions (O_2^-) and photo-induced oxygen anions ($O^-_{2(h\nu)}$), leading to the formation of water molecules and releasing the electrons to the depletion area under visible light (Eqs. (4) and (5)) [34].

$$\text{In air: } O_{2\ (ads)} + e^- \rightarrow O_2^- \quad (1)$$

$$\text{Under LED light: } h\nu \rightarrow h^+ + e^-_{(h\nu)} \quad (2)$$

$$O_2 + e^-_{(h\nu)} \rightarrow O^-_{2(h\nu)} \quad (3)$$

$$\text{In hydrogen: } O_2^- + 2H_2 \rightarrow 2H_2O + e^- \quad (4)$$

$$O^-_{2(h\nu)} + 2H_2 \rightarrow 2H_2O + e^- \quad (5)$$

The improved performance of the $Au_{nanorod}$@ZnO CS-NPs sensor was attributed to the LSPR and electronic sensitization effects of Au NRs core. With the introduction of Au NRs, since the work function of Au NRs (3.92 eV) was larger than that of ZnO (3.72 eV) (Fig. S15), leading to the electrons transferred from the ZnO shell to the Au core (Fig. 7). This was the reason why the $Au_{nanorod}$@ZnO sensor showed a baseline resistance (R_a) higher than that pure ZnO sensor. With the introduction of 650 nm red light, the response value of the $Au_{nanorod}$@ZnO sensor was enhanced. This was because the periodic oscillation of localized surface electrons was produced due to the interaction between incident photons and Au NRs. The LSPR effect arising from this interaction enhanced the local electric field at the $Au_{nanorod}$@ZnO interface, thereby increasing the light absorption efficiency for the ZnO sensitive materials [67]. The excitation of the longitudinal LSPR generates a stronger localized electromagnetic field and more efficient plasmon-induced electron transfer from Au nanorods to ZnO than that of Au nanospheres. This process reduces the electron depletion layer and lowers the electrical resistance of the $Au_{nanorod}$@ZnO sensor at room temperature. When hydrogen gas is supplied here, the electrical resistance of this sensor further decreases (Fig. 7). In addition, Au NRs acted as a good catalyst for the dissociation and ionization of hydrogen molecules (H_2) into hydrogen atoms (H) (Eq. (6)) due to the spillover effect [34,76]. These hydrogen atoms easily reacted with O_2^- and $O^-_{2(h\nu)}$ and released electrons to the ZnO shell (Eqs. (7) and (8)). Therefore, the electrical resistance of the sensor in the presence of hydrogen gas was reduced, improving it overall gas sensing performance.

$$H_2 \rightarrow 2H \quad (6)$$

$$O_2^- + 4H \rightarrow 2H_2O + e^- \quad (7)$$

$$O^-_{2(h\nu)} + 4H \rightarrow 2H_2O + e^- \quad (8)$$

Moreover, the higher surface area, larger pore volume, increased oxygen vacancy/chemisorbed oxygen content, and Au nanorod morphology are also beneficial for gas sensing because they provide more active sites and facilitate gas diffusion. These factors may contribute to the enhanced sensing performance.

4. Conclusion

In this study, the $Au_{nanorod}$@ZnO CS-NPs were successfully prepared

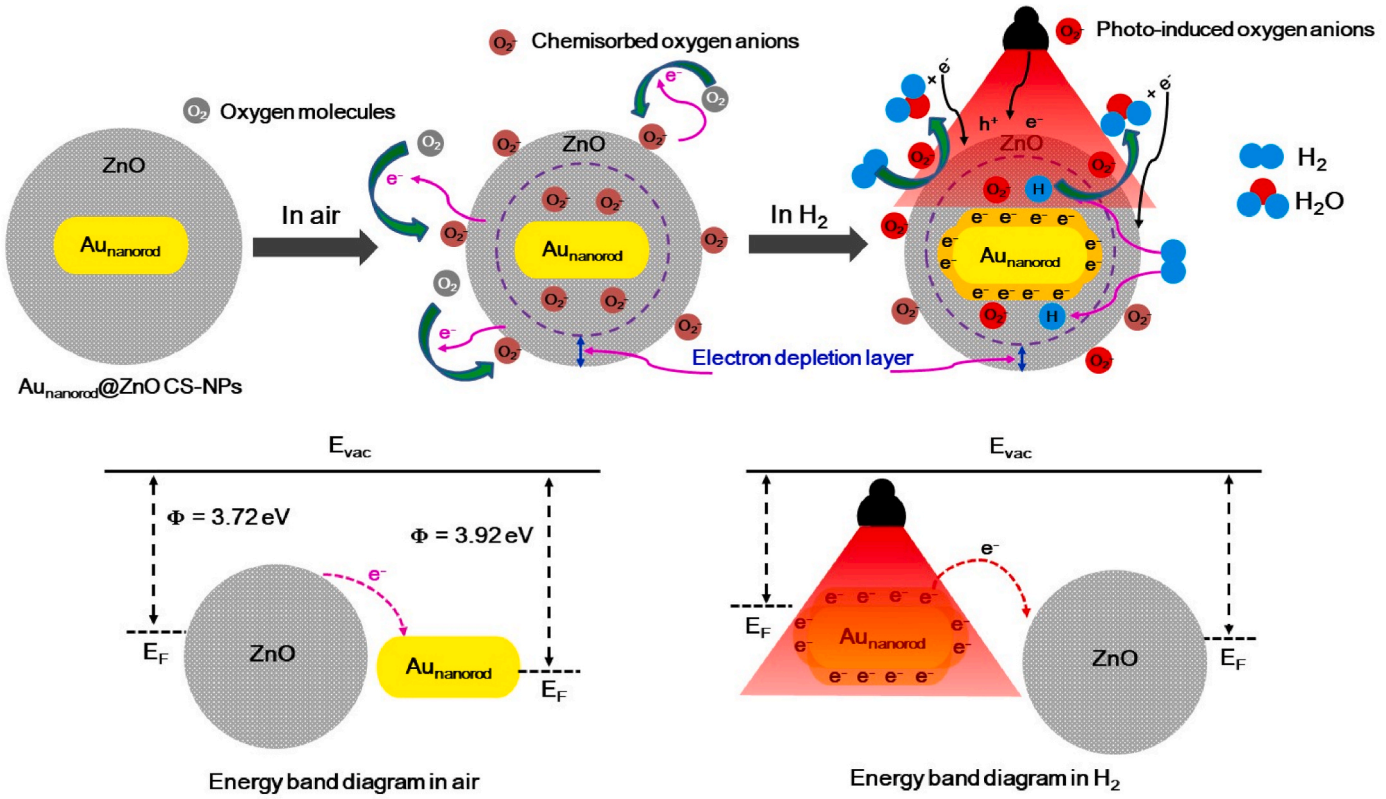


Fig. 7. Surface reaction mechanism based on electronic sensitization and LSPR effect of $Au_{nanorod}$@ZnO CS-NPs sensor in air and hydrogen environment.

by the hydrothermal method and the effect the shape of the Au core on the hydrogen gas sensing properties at room temperature was investigated. The LSPR properties of Au NRs enhanced the absorption in the visible light range, providing sufficient energy to promote the sensor response compared to pure ZnO and $Au_{nanosphere}$@ZnO sensors. The LSPR effect of Au NRs in the $Au_{nanorod}$@ZnO sensor extended the light absorption wavelength of ZnO NPs from blue to green and red lights. The $Au_{nanorod}$@ZnO CS-NPs sensor showed an excellent response (6.26) to 100 ppm hydrogen gas at room temperature using red light (650 nm). Moreover, the $Au_{nanorod}$@ZnO sensor exhibited superior selectivity towards hydrogen against other target gases, including CH_3CHO, C_2H_5OH, CH_4, and CO. The enhanced hydrogen sensing performance of the $Au_{nanorod}$@ZnO CS-NPs sensor is likely associated with the combined contributions of LSPR mediated photoactivation, electronic sensitization induced by the Au nanorod core, specific surface area, pore volume, oxygen vacancy/chemisorbed oxygen content, and Au nanorod morphology.

5. Notes

The authors declare no competing financial interest.

Declaration of competing interest

The authors declare that they have no known competing financial interests or personal relationships that could have appeared to influence the work reported in this paper.

Acknowledgements

This work was supported by 1) the National Research Foundation of Korea (NRF) and the Commercialization Promotion Agency for R&D Outcomes (COMPA) grant funded by the Korean government (Ministry of Science and ICT) (RS-2025-02314407), 2) the Regional Innovation System & Education (RISE) initiative, funded by the Ministry of Education and administered by the National Research Foundation of Korea (NRF), and 3) the National Research Foundation of Korea (NRF) grant funded by the Korean government (MSIP) (RS-2026-25482529).

Appendix A. Supplementary data

Supplementary data to this article can be found online at https://doi.org/10.1016/j.mtnano.2026.100972.

Data availability

Data will be made available on request.

References

[1] R. Bhandari, N. Adhikari, A comprehensive review on the role of hydrogen in renewable energy systems, Int. J. Hydrogen Energy 82 (2024) 923–951, https://doi.org/10.1016/j.ijhydene.2024.08.004.
[2] T. Thathsara, J. Meilak, M. Sangchap, C. Harrison, R. Hocking, M. Shafiei, Visible light active rGO nanosheet encapsulated Pd quantum-sized dots decorated TiO2 nano-spheres for hydrogen gas sensing at low temperatures, Int. J. Hydrogen Energy 48 (2023) 33358–33371, https://doi.org/10.1016/j.ijhydene.2023.05.061.
[3] L. Boon-Brett, J. Bousek, G. Black, P. Moretto, P. Castello, T. Hübert, U. Banach, Identifying performance gaps in hydrogen safety sensor technology for automotive and stationary applications, Int. J. Hydrogen Energy 35 (2010) 373–384, https://doi.org/10.1016/j.ijhydene.2009.10.064.
[4] T. Hübert, L. Boon-Brett, G. Black, U. Banach, Hydrogen sensors - a review, Sens. Actuators, B Chem. 157 (2011) 329–352, https://doi.org/10.1016/j.snb.2011.04.070.
[5] A. Yavari, C.J. Harrison, S.A. Gorji, M. Shafiei, Hydrogen 4.0: a cyber–physical system for renewable hydrogen energy plants, Sensors 24 (2024) 1–28, https://doi.org/10.3390/s24103239.
[6] R. Ono, M. Nifuku, S. Fujiwara, S. Horiguchi, T. Oda, Minimum ignition energy of hydrogen-air mixture: effects of humidity and spark duration, J. Electrost. 65 (2007) 87–93, https://doi.org/10.1016/j.elstat.2006.07.004.
[7] W.J. Buttner, M.B. Post, R. Burgess, C. Rivkin, An overview of hydrogen safety sensors and requirements, Int. J. Hydrogen Energy 36 (2011) 2462–2470, https://doi.org/10.1016/j.ijhydene.2010.04.176.

[8] R. Ishihara, Y. Yamaguchi, K. Tanabe, Y. Makino, K. Nishio, Preparation of Pt/WO 3 -coated polydimethylsiloxane membrane for transparent/flexible hydrogen gas sensors, Mater. Chem. Phys. 226 (2019) 226–229, https://doi.org/10.1016/j.matchemphys.2018.12.052.

[9] O. Casals Qomaruddin, H.S. Wasisto, A. Waag, J.D. Prades, C. Fàbrega, Visible-light-driven room temperature NO2 gas sensor based on localized surface plasmon resonance: the case of gold nanoparticle decorated zinc oxide nanorods (ZnO NRs), Chemosensors 10 (2022), https://doi.org/10.3390/chemosensors10010028.

[10] H. Huang, H. Gong, C.L. Chow, J. Guo, T.J. White, M.S. Tse, O.K. Tan, Low-temperature growth of SnO2 nanorod arrays and tunable n-p-n sensing response of a ZnO/SnO2 heterojunction for exclusive hydrogen sensors, Adv. Funct. Mater. 21 (2011) 2680–2686, https://doi.org/10.1002/adfm.201002115.

[11] G. Korotcenkov, S. Do Han, J.R. Stetter, Review of electrochemical hydrogen sensors, Chem. Rev. 109 (2009) 1402–1433, https://doi.org/10.1021/cr800339k.

[12] S. Panda, S. Mehlawat, N. Dhariwal, A. Sanger, A. Kumar, Comprehensive review on gas sensors: unveiling recent developments and addressing challenges, Mater. Sci. Eng., B 308 (2024) 117616, https://doi.org/10.1016/j.mseb.2024.117616.

[13] T. Hübert, L. Boon-Brett, V. Palmisano, M.A. Bader, Developments in gas sensor technology for hydrogen safety, Int. J. Hydrogen Energy 39 (2014) 20474–20483, https://doi.org/10.1016/j.ijhydene.2014.05.042.

[14] J. Hu, S. Dou, X. Liu, B. Liu, X. Xue, Y. Zhang, Full-spectrum solar light–activated chemiresistive sensors based on W18O49/Ag2S S-Scheme heterostructure for highly sensitive room-temperature NO2 detection, Rare Met. 45 (2026), https://doi.org/10.1002/rar2.70439.

[15] J.-Y. Hu, H. Lei, H.-Y. Zhang, X.-X. Xue, X.-P. Wang, C.-H. Wang, Y. Zhang, High Reliable Gas Sensor Based on crystal-facet Regulated a-Fe 2 O 3 Nanocrystals for Rapid Detection of Exhaled Acetone, (n.d.). https://doi.org/10.1007/s12598.

[16] T.T. Wang, B.S. Xing, C.Y. Guo, J.Y. Hao, Y. Wang, L.H. Huo, X.L. Cheng, Y.M. Xu, Recent advances of emerging tin disulfide for room temperature gas sensing, Rare Met. 42 (2023) 3897–3913, https://doi.org/10.1007/s12598-023-02484-w.

[17] J. Hu, X. Liu, J. Zhang, X. Gu, Y. Zhang, Plasmon-activated NO2 sensor based on Au@MoS2 core-shell nanoparticles with heightened sensitivity and full recoverability, Sens. Actuators, B Chem. 382 (2023), https://doi.org/10.1016/j.snb.2023.133505.

[18] J. Hu, X. Wang, H. Lei, M. Luo, Y. Zhang, Plasmonic photothermal driven MXene-based gas sensor for highly sensitive NO2 detection at room temperature, Sens. Actuators, B Chem. 407 (2024), https://doi.org/10.1016/j.snb.2024.135422.

[19] J. Hu, Y. Zhao, Q. Wang, Y. Zhang, Full-spectrum visible light driven chemiresistive sensor based on g-C3N4/SnS/Au heterostructures for reliable NO2 detection at room temperature, Sens. Actuators, B Chem. 442 (2025), https://doi.org/10.1016/j.snb.2025.138103.

[20] Y. Wang, L. Duan, Z. Deng, J. Liao, Electrically transduced gas sensors based on semiconducting metal oxide nanowires, Sensors (Switzerland) 20 (2020) 1–41, https://doi.org/10.3390/s20236781.

[21] N.A. Isaac, I. Pikaar, G. Biskos, Metal oxide semiconducting nanomaterials for air quality gas sensors: operating principles, performance, and synthesis techniques, Microchim. Acta 189 (2022), https://doi.org/10.1007/s00604-022-05254-0.

[22] Y.K. Gautam, K. Sharma, S. Tyagi, A.K. Ambedkar, M. Chaudhary, B. Pal Singh, Nanostructured metal oxide semiconductor-based sensors for greenhouse gas detection: progress and challenges, R. Soc. Open Sci. 8 (2021), https://doi.org/10.1098/rsos.201324.

[23] M.Z. Atashbar, G. Korotcenkov, S. Krishnamurthy, Basic principles of chemical sensors operation B, chemical sensors: fundamental of sensing materials. https://www.researchgate.net/publication/286451678, 2009.

[24] R.A.B. John, A. Ruban Kumar, A review on resistive-based gas sensors for the detection of volatile organic compounds using metal-oxide nanostructures, Inorg. Chem. Commun. 133 (2021) 108893, https://doi.org/10.1016/j.inoche.2021.108893.

[25] A. Mirzaei, H.R. Yousefi, F. Falsafi, M. Bonyani, J.H. Lee, J.H. Kim, H.W. Kim, S. S. Kim, An overview on how Pd on resistive-based nanomaterial gas sensors can enhance response toward hydrogen gas, Int. J. Hydrogen Energy 44 (2019) 20552–20571, https://doi.org/10.1016/j.ijhydene.2019.05.180.

[26] Z. Li, Z.J. Yao, A.A. Haidry, T. Plecenik, L.J. Xie, L.C. Sun, Q. Fatima, Resistive-type hydrogen gas sensor based on TiO2: a review, Int. J. Hydrogen Energy 43 (2018) 21114–21132, https://doi.org/10.1016/j.ijhydene.2018.09.051.

[27] B. Saruhan, R. Lontio Fomekong, S. Nahirniak, Review: influences of semiconductor metal oxide properties on gas sensing characteristics, Frontiers in Sensors 2 (2021) 1–24, https://doi.org/10.3389/fsens.2021.657931.

[28] V. Aroutiounian, Metal oxide hydrogen, oxygen, and carbon monoxide sensors for hydrogen setups and cells, Int. J. Hydrogen Energy 32 (2007) 1145–1158, https://doi.org/10.1016/j.ijhydene.2007.01.004.

[29] C. Yao, L. Wu, H. Li, N. Xu, J. Sun, J. Wu, WS2 coating and Au nanoparticle decoration of ZnO nanorods for improving light-activated NO2 sensing, Appl. Surf. Sci. 584 (2022), https://doi.org/10.1016/j.apsusc.2022.152508.

[30] Y. Kang, F. Yu, L. Zhang, W. Wang, L. Chen, Y. Li, Review of ZnO-based nanomaterials in gas sensors, Solid State Ionics 360 (2021) 115544, https://doi.org/10.1016/j.ssi.2020.115544.

[31] B. Mondal, B. Basumatari, J. Das, C. Roychaudhury, H. Saha, N. Mukherjee, ZnO-SnO2 based composite type gas sensor for selective hydrogen sensing, Sens. Actuators, B Chem. 194 (2014) 389–396, https://doi.org/10.1016/j.snb.2013.12.093.

[32] Y. Shi, H. Xu, T. Liu, S. Zeb, Y. Nie, Y. Zhao, C. Qin, X. Jiang, Advanced development of metal oxide nanomaterials for H2 gas sensing applications, Mater. Adv. 2 (2021) 1530–1569, https://doi.org/10.1039/d0ma00880j.

[33] C. Lupan, R. Khaledialidusti, A.K. Mishra, V. Postica, M.I. Terasa, N. Magariu, T. Pauporté, B. Viana, J. Drewes, A. Vahl, F. Faupel, R. Adelung, Pd-Functionalized zno:eu columnar films for room-temperature hydrogen gas sensing: a combined experimental and computational approach, ACS Appl. Mater. Interfaces 12 (2020) 24951–24964, https://doi.org/10.1021/acsami.0c02103.

[34] S.K.T. Thathsara, C.J. Harrison, R.K. Hocking, M. Shafiei, Photoactive semiconducting metal oxides: hydrogen gas sensing mechanisms, Int. J. Hydrogen Energy 47 (2022) 18208–18227, https://doi.org/10.1016/j.ijhydene.2022.04.038.

[35] J. Wang, S. Fan, Y. Xia, C. Yang, S. Komarneni, Room-temperature gas sensors based on ZnO nanorod/Au hybrids: visible-light-modulated dual selectivity to NO2 and NH3, J. Hazard Mater. 381 (2020) 120919, https://doi.org/10.1016/j.jhazmat.2019.120919.

[36] O. Casals, A. Šutka, T. Granz, A. Waag, H.S. Wasisto, J.D. Prades, F. Cristian, Visible Light-Driven P -type Semiconductor Gas Sensors Based on Cafe 2 O 4 Nanoparticles †, (n.d.) 1–12.

[37] R. Vargas-Bernal, Electrical properties of two-dimensional materials used in gas sensors, Sensors (Switzerland) 19 (2019) 100–107, https://doi.org/10.3390/s19061295.

[38] N.D. Chinh, T.T. Hien, L. Do Van, N.M. Hieu, N.D. Quang, S.M. Lee, C. Kim, D. Kim, Adsorption/desorption kinetics of nitric oxide on zinc oxide nano film sensor enhanced by light irradiation and gold-nanoparticles decoration, Sens. Actuators, B Chem. 281 (2019) 262–272, https://doi.org/10.1016/j.snb.2018.10.113.

[39] Q. Zhang, G. Xie, M. Xu, Y. Su, H. Tai, H. Du, Y. Jiang, Visible light-assisted room temperature gas sensing with ZnO-Ag heterostructure nanoparticles, Sens. Actuators, B Chem. 259 (2018) 269–281, https://doi.org/10.1016/j.snb.2017.12.052.

[40] F. Xu, H.F. Lv, S.Y. Wu, H.P. Ho, Light-activated gas sensing activity of ZnO nanotetrapods enhanced by plasmonic resonant energy from Au nanoparticles, Sens. Actuators, B Chem. 259 (2018) 709–716, https://doi.org/10.1016/j.snb.2017.12.128.

[41] S.J. Young, Y.H. Liu, Y.L. Chu, J.Z. Huang, Nonenzymatic Glucose Sensors of ZnO Nanorods Modified by Au Nanoparticles, IEEE Sens. J. 23 (2023) 12503–12510, https://doi.org/10.1109/JSEN.2023.3272778.

[42] Y.H. Liu, S.J. Young, L.W. Ji, Y.L. Chu, S.J. Chang, High-sensitive ethanol gas sensor using Ag modified ZnO nanosheets, Talanta Open 10 (2024), https://doi.org/10.1016/j.talo.2024.100386.

[43] S.J. Young, Y.L. Chu, Hydrothermal Synthesis and Improved CH_3OH-Sensing Performance of ZnO Nanorods with Adsorbed Au NPs, IEEE Trans. Electron. Dev. 68 (2021) 1886–1891, https://doi.org/10.1109/TED.2021.3060354.

[44] Sheng-Joue Young, Yen-Lin Chu, Platinum nanoparticle-decorated ZnO nanorods improved the performance of methanol gas sensor, J. Electrochem. Soc. 167 (2020).

[45] Y.L. Chu, S.J. Young, L.W. Ji, T.T. Chu, K.T. Lam, Y.J. Hsiao, I.T. Tang, T.H. Kuo, Characteristics of gas sensors based on Co-Doped ZnO nanorod arrays, J. Electrochem. Soc. 167 (2020).

[46] Y.T. Tsai, S.J. Chang, L.W. Ji, Y.J. Hsiao, I.T. Tang, H.Y. Lu, Y.L. Chu, High sensitivity of NO gas sensors based on novel Ag-Doped ZnO nanoflowers enhanced with a UV light-emitting diode, ACS Omega 3 (2018) 13798–13807, https://doi.org/10.1021/acsomega.8b01882.

[47] D. Qu, B. Cheng, X. Shao, J. Hu, S. Bai, Y. Zhang, W. Wu, H. Haick, Advances in metals and metal hybrids-based gas sensors and their applications, Rare Met. 44 (2025) 9363–9413, https://doi.org/10.1007/s12598-025-03527-0.

[48] Y.-X. Wang, B. Liu, B.-H. Liu, Y. Zhang, Oxygen-Assisted Recoverable Hydrogen Sensor Based on Sensing Gate Field Effect Transistor with ppb-level Detection Ability, (n.d.). https://doi.org/10.1007/s12598.

[49] T. Bora, D. Zoepfl, J. Dutta, Importance of plasmonic heating on visible light driven photocatalysis of gold nanoparticle decorated zinc oxide nanorods, Sci. Rep. 6 (2016) 1–10, https://doi.org/10.1038/srep26913.

[50] J. Gong, Y. Li, Y. Deng, UV and visible light controllable depletion zone of ZnO-polyaniline p-n junction and its application in a photoresponsive sensor, Phys. Chem. Chem. Phys. 12 (2010) 14864–14867, https://doi.org/10.1039/c0cp01101k.

[51] Y.-L. Chu, S.-J. Young, T.-T. Chu, A. Khosla, K.-Y. Chiang, L.-W. Ji, Improvement of the UV-Sensing performance of Ga-Doped ZnO nanostructures via a wet chemical solution at room temperature, ECS J. Solid State Sci. Technol. 10 (2021) 127001, https://doi.org/10.1149/2162-8777/ac3e43.

[52] Y.L. Chu, S.J. Young, L.W. Ji, I.T. Tang, T. Te Chu, Fabrication of ultraviolet photodetectors based on Fe-doped ZnO nanorod structures, Sensors (Switzerland) 20 (2020) 1–12, https://doi.org/10.3390/s20143861.

[53] C. Liow, F. Meng, X. Chen, S. Li, Dependence of plasmonic properties on electron densities for various coupled Au nanostructures, J. Phys. Chem. C 118 (2014) 27531–27538, https://doi.org/10.1021/jp5099975.

[54] P. Pimpang, A.S. Zoolfakar, R.A. Rani, R.A. Kadir, D. Wongratanaphisan, A. Gardchareon, K. Kalantar-zadeh, S. Choopun, Hydrogen sensors based on gold nanoclusters assembled onto ZnO nanostructures at low operating temperature, Ceram. Int. 43 (2017) S511–S515, https://doi.org/10.1016/j.ceramint.2017.05.259.

[55] Jinyong Hu, Enduo Hu, Xinyao Liu, Bohao Liu, Yong Zhang, Multigas selective identification based on a single chemiresistive gas sensor via dynamic light-pulse modulation and machine learning, ACS Sens. 11 (2026) 4799–4810.

[56] V.S. Sanjana Devi, B. Balraj, S. Amuthameena, T. Joby Titus, Enhanced hydrogen gas sensing performance of gold nanoparticle decorated nitrogen-doped ZnO nanomaterials for improved sensitivity and rapid response, IEEE Trans. Nanotechnol. 24 (2025) 27–33, https://doi.org/10.1109/TNANO.2024.3522368.

[57] Y. Chen, H. Ming, Review of surface plasmon resonance and localized surface plasmon resonance sensor? Photonic Sensors 2 (2012) 37–49, https://doi.org/10.1007/s13320-011-0051-2.

[58] Y.L. Chu, Y.H. Liu, T. Te Chu, S.J. Young, Improved UV-Sensing of Au-Decorated ZnO nanostructure MSM photodetectors, IEEE Sens. J. 22 (2022) 5644–5650, https://doi.org/10.1109/JSEN.2022.3150254.
[59] Y.L. Chu, S.J. Young, Y.R. Huang, S. Arya, T. Te Chu, Highly Sensitive Ethanol Gas Sensors of Au Nanoparticle-Adsorbed ZnO Nanorod Arrays via a Photochemical Deposition Treatment, ACS Appl. Electron. Mater. 7 (2025) 2327–2338, https://doi.org/10.1021/acsaelm.4c02091.
[60] Y.L. Chu, Y.R. Huang, C.H. Tung, S. Arya, T. Te Chu, S.J. Young, Pd nanoparticles decorated on 1-D ZnO nanostructures for highly sensitive C2H5OH gas sensors synthesised by a novel photochemical deposition process under UV light irradiation, Ceram. Int. (2026), https://doi.org/10.1016/j.ceramint.2026.05.299.
[61] Jun Zhou, Jianshuo Zhang, Haitao Yang, Zhuan Wang, Jin-an Shi, Wu Zhou, Nan Jiang, Guoyu Xian, Qi Qi, Yuxiang Weng, Chengmin Shen, Zhaohua Cheng, Shengtai He, Plasmon-induced hot electron transfer in Au–ZnO heterogeneous nanorods for enhanced SERS, Nanoscale 11 (2019).
[62] M.E. Aguirre, A. Armanelli, G. Perelstein, A. Feldhoff, A.J. Tolley, M.A. Grela, Modulation of the electron transfer processes in Au–ZnO nanostructures, Nanoscale 7 (2015).
[63] S. Jayabal, A. Pandikumar, H.N. Lim, R. Ramaraj, T. Sun, N.M. Huang, A gold nanorod-based localized surface plasmon resonance platform for the detection of environmentally toxic metal ions, Analyst 140 (2015) 2540–2555, https://doi.org/10.1039/c4an02330g.
[64] N. Zhou, H. Zhu, S. Li, J. Yang, T. Zhao, Y. Li, Q.H. Xu, Au Nanorod/ZnO Core-Shell Nanoparticles as Nano-Photosensitizers for Near-Infrared Light-Induced Singlet Oxygen Generation, J. Phys. Chem. C 122 (2018) 7824–7830, https://doi.org/10.1021/acs.jpcc.7b12463.
[65] A.P. Ivanishcheva, V.V. Sysoev, K.A. Abdullin, A.V. Nesterenko, S.A. Khubezhov, V. V. Petrov, The application of combined visible and ultraviolet irradiation to improve the functional characteristics of gas sensors based on ZnO/SnO2 and ZnO/Au nanorods, Chemosensors 11 (2023), https://doi.org/10.3390/chemosensors11030200.
[66] P. Shanmugam, G.P. Kuppuswamy, D. Chidambaram, R. Kalidoss, A. Sundaramurthy, Y. Sivalingam, Influence of gas adsorption on the surface photovoltage of Au nanorods embedded polymer coated ZnO nanorods under visible light irradiation, Ceram. Int. 48 (2022) 29158–29164, https://doi.org/10.1016/j.ceramint.2022.05.091.
[67] Y. Sun, J. Hu, Y. Zhang, Visible light assisted trace gaseous NO2 sensor with anti-humidity ability via LSPR enhancement effect, Sens. Actuators, B Chem. 367 (2022) 132032, https://doi.org/10.1016/j.snb.2022.132032.
[68] T.K. Sau, C.J. Murphy, Seeded high yield synthesis of short Au nanorods in aqueous solution, Langmuir 20 (2004) 6414–6420, https://doi.org/10.1021/la049463z.
[69] T. Van Tran, M.J. Ahemad, D.S. Kim, T.D. Le, V. Dao, Y.T. Yu, Ultra high response for hydrogen gas on Pd–Augr-alloy@ZnO core-shell nanoparticles with Pd–Au gradient composition alloy core, Mater. Today Nano 21 (2023), https://doi.org/10.1016/j.mtnano.2022.100292.
[70] P.R. Chikate, K.D. Daware, S.S. Patil, P.N. Didwal, G.S. Lole, R.J. Choudhary, S. W. Gosavi, R.S. Devan, Effects of Au loading on the enhancement of photoelectrochemical activities of the Au@ZnO nano-heteroarchitecture, New J. Chem. 44 (2020) 5535–5544, https://doi.org/10.1039/d0nj00004c.
[71] H. Wu, Q. Fu, Y. Li, Y. Cui, R. Wang, N. Su, L. Lin, A. Dong, Y. Ning, F. Yang, X. Bao, Controlled growth of uniform two-dimensional ZnO overlayers on Au(111) and surface hydroxylation, Nano Res. 12 (2019) 2348–2354, https://doi.org/10.1007/s12274-019-2373-0.
[72] E. Wongrat, N. Chanlek, C. Chueaiarrom, B. Samransuksamer, N. Hongsith, S. Choopun, Low temperature ethanol response enhancement of ZnO nanostructures sensor decorated with gold nanoparticles exposed to UV illumination, Sens. Actuators A Phys. 251 (2016) 188–197, https://doi.org/10.1016/j.sna.2016.10.022.
[73] D. Ramírez-Ortega, D. Guerrero-Araque, P. Acevedo-Peña, E. Reguera, H. A. Calderon, R. Zanella, Enhancing the photocatalytic hydrogen production of the ZnO–TiO2 heterojunction by supporting nanoscale Au islands, Int. J. Hydrogen Energy 46 (2021) 34333–34343, https://doi.org/10.1016/j.ijhydene.2021.08.019.
[74] Y. Cheng, S. Lu, W. Xu, H. Wen, J. Wang, Fabrication of superhydrophobic Au-Zn alloy surface on a zinc substrate for roll-down, self-cleaning and anti-corrosion properties, J. Mater. Chem. A Mater 3 (2015) 16774–16784, https://doi.org/10.1039/c5ta03979g.
[75] A. Bumajdad, M. Madkour, Y. Abdel-Moneam, M. El-Kemary, Nanostructured mesoporous Au/TiO2 for photocatalytic degradation of a textile dye: the effect of size similarity of the deposited Au with that of TiO2 pores, J. Mater. Sci. 49 (2014) 1743–1754, https://doi.org/10.1007/s10853-013-7861-0.
[76] S.M. Majhi, P. Rai, Y.T. Yu, Facile approach to synthesize Au@ZnO core-shell nanoparticles and their application for highly sensitive and selective gas sensors, ACS Appl. Mater. Interfaces 7 (2015) 9462–9468, https://doi.org/10.1021/acsami.5b00055.